Monthly Notices
of the
ROYAL ASTRONOMICAL SOCIETY

Mon. Not. R. Astron. Soc. **415,** 2580–2593 (2011) doi:10.1111/j.1365-2966.2011.18881.x

Detecting neutral hydrogen in emission at redshift $z \simeq 1$

Nishikanta Khandai,[1⋆] Shiv K. Sethi,[1,2] Tiziana Di Matteo,[1] Rupert A.C. Croft,[1] Volker Springel,[3,4] Anirban Jana[5] and Jeffrey P. Gardner[6]

[1]*McWilliams Center for Cosmology, Carnegie Mellon University, 5000 Forbes Avenue, Pittsburgh, PA 15213, USA*
[2]*Raman Research Institute, C. V. Raman Avenue, Sadashivanagar, Bangalore 560080, India*
[3]*Heidelberg Institute for Theoretical Studies, Schloss-Wolfsbrunnenweg 35, 69118 Heidelberg, Germany*
[4]*Astronomisches Recheninstitut, Zentrum für Astronomie der Universität Heidelberg, Mönchhofstr. 12-14, 69120 Heidelberg, Germany*
[5]*Pittsburgh Supercomputing Center, 300 S. Craig Street, Pittsburgh, PA 15213, USA*
[6]*Department of Physics, University of Washington, Seattle, Box 351560, WA 98195-1560, USA*

Accepted 2011 April 8. Received 2011 February 26; in original form 2010 December 8

ABSTRACT

We use a large N-body simulation to examine the detectability of H I in emission at redshift $z \simeq 1$, and the constraints imposed by current observations on the neutral hydrogen mass function of galaxies at this epoch. We consider three different models for populating dark matter haloes with H I, designed to encompass uncertainties at this redshift. These models are consistent with recent observations of the detection of H I in emission at $z \simeq 0.8$. Whilst detection of 21-cm emission from individual haloes requires extremely long integrations with existing radio interferometers, such as the Giant Meter Radio Telescope (GMRT), we show that the stacked 21-cm signal from a large number of haloes can be easily detected. However, the stacking procedure requires accurate redshifts of galaxies. We show that radio observations of the field of the Deep Extragalactic Evolutionary Probe 2 (DEEP2) spectroscopic galaxy redshift survey should allow detection of the H I mass function at the 5–12σ level in the mass range $10^{11.4}\,h^{-1}\,\mathrm{M}_{\odot} \leq M_{\rm halo} \leq 10^{12.5}\,h^{-1}\,\mathrm{M}_{\odot}$, with a moderate amount of observation time. Assuming a larger noise level that corresponds to an upper bound for the expected noise for the GMRT, the detection significance for the H I mass function is still at the 1.7–3σ level. We find that optically undetected satellite galaxies enhance the H I emission profile of the parent halo, leading to broader wings as well as a higher peak signal in the stacked profile of a large number of haloes. We show that it is in principle possible to discern the contribution of undetected satellites to the total H I signal, even though cosmic variance limitation make this challenging for some of our models.

Key words: galaxies: evolution – large-scale structure of Universe – radio lines: galaxies.

1 INTRODUCTION

Observations show that the cosmic star formation rate (SFR) has declined by more than an order of magnitude since $z \simeq 1$ (Hopkins 2004). However, a combined census of the cold gas, the fuel for star formation and stellar components is still largely missing in observations. The cold gas fraction of a halo is a crucial ingredient in models of galaxy formation and constitutes the link to how galaxies obtain gas and subsequently convert it to stars. Hence, measurements of H I in the post-reionization era can place tight constraints on different models of galaxy formation (Putman et al. 2009).

After the epoch of reionization, the neutral hydrogen (H I) survives in dense clouds, e.g. damped Lyman α systems (DLAs) and Lyman limit systems, that are high-redshift equivalents of the H I-rich galaxies that we see at the present epoch. The baryon fraction locked up in H I, $\Omega_{\rm H\,I}$, in star-forming galaxies in the post-reionization epoch can be determined from the study of DLAs in absorption for $0.5 \leq z \leq 5$ (Prochaska, Herbert-Fort & Wolfe 2005; Rao, Turnshek & Nestor 2006; Noterdaeme et al. 2009). Even though these observations give clues about aggregate behaviour of star formation as a function of redshift, they cannot be used to infer the total H I mass of these systems because they are seen in absorption. At $z \simeq 1$, even the detection of H I in DLA has not been easy as the Lyman α frequency is not accessible to ground-based telescopes. At this redshift, constraints on the global H I fraction come from associated Mg II systems, *Hubble Space Telescope* observations (for details see Rao et al. 2006, and references therein) and the absorption of 21-cm radiation from bright background radio sources (Kanekar et al. 2009), but with significant uncertainties on the estimated H I fraction. Direct observation of H I in emission

⋆E-mail: nkhandai@andrew.cmu.edu

and its detailed modelling has only been possible at $z \simeq 0$ thus far (Zwaan et al. 2005).

Direct observation in 21-cm emission of 10 massive galaxies have been reported for $0.17 < z < 0.25$, with the Arecibo Telescope (Catinella et al. 2008). At higher redshifts, the H I emission from individual clouds is too weak to be detectable with present radio instruments (Bagla, Khandai & Datta 2010). A long integration time is required for detecting even the brightest objects since the peak signal is a few tens of μJy, whereas the system noise is of the order of hundreds of μJy. A possible approach to circumvent the difficulty of detecting individual clouds lies in stacking the H I emission of galaxies with known redshifts. This approach has been attempted for both cluster galaxies and the field galaxies in the recent past (Lah et al. 2007, 2009). In particular, a similar line of study has resulted in the recent detection of H I at $z \simeq 0.8$ (Chang et al. 2010). An alternative approach rests on the possible detection of the fluctuation in the redshifted H I emission from high redshifts (Bharadwaj & Sethi 2001; Chang et al. 2008; Bharadwaj, Sethi & Saini 2009).

On the theoretical side, semi-analytical models of galaxy formation have looked at the evolution of cold gas (both in atomic and molecular form) in galaxies and their results match with observations at $z = 0$ (Obreschkow & Rawlings 2009a; Obreschkow et al. 2009a,b; Obreschkow & Rawlings 2009b; Fu et al. 2010; Kim et al. 2011; Power, Baugh & Lacey 2010). However, observations at higher redshifts are needed to better constrain the evolution of cold gas predicted by these models.

Given the importance of connecting cold gas and stars at $z \simeq 1$ over a wide range of galaxy environments, it is crucial to make predictions for various detection strategies for current and upcoming telescopes. In this work we focus on the stacking method of individual galaxies with known redshifts to predict how well the H I mass function at $z = 1$ can be constrained with existing surveys and telescopes [in particular, the DEEP2[1] survey and the Giant Meter Radio Telescope (GMRT);[2] but note that our method is generic and can be extended to future surveys and instruments]. By stacking we can also study the contribution of small satellite galaxies, which are undetected in an optical survey but (as we shall show) contain non-negligible amounts of H I, to the total 21-cm signal in emission and also examine the constraints that one can put on the H I mass function.

We model the H I in dark matter (DM) haloes in a large N-body simulation by refining the model of Bagla et al. (2010). Given the paucity of observations at the redshifts under consideration, and our limited understanding of how H I populates DM haloes at these redshifts, we consider a variety of models. These are constrained by observations of H I at low redshift, simulations of DLAs in small volumes at high redshift, as well as by some results of semi-analytical models of galaxy formation at intermediate redshifts. In particular, the models that we consider are consistent with recent observations of H I in emission at $z \simeq 0.8$ (Chang et al. 2010).

Our paper is organized as follows. We present our large DM simulation in Section 2, and describe our model for the H I distribution in the simulation along with specifications of the DEEP2 survey as well as the GMRT in Section 3. We discuss our stacking procedure of individual galaxies and the contribution of undetected satellites to the stacked H I spectra in Section 4. In Section 5, we present our results and discuss the prospects of detection with the GMRT, and the constraints that one can put on the H I mass function. We revisit the issue of undetected satellites and its effect on the H I mass function and discuss whether their presence can be detected. Finally, we present our conclusions in Section 6.

[1] http://deep.berkeley.edu
[2] http://gmrt.ncra.tifr.res.in

Table 1. Basic simulation parameters for our DM run. The columns list the size of the simulation box, $L_{\rm box}$, the number of DM particles used in the simulation, $N_{\rm part}$, the mass of a single DM particle, $m_{\rm DM}$, and the gravitational softening length, ϵ. All length-scales are in comoving units.

$L_{\rm box}$ (h^{-1} Mpc)	$N_{\rm part}$	$m_{\rm DM}$ ($10^8\,h^{-1}\,{\rm M}_\odot$)	ϵ (h^{-1} kpc)
400	2448^3	3.1	6.5

2 *N*-BODY SIMULATION

We have used P-GADGET, a significantly upgraded version of GADGET2 (Springel 2005) which we are developing for upcoming petascale supercomputer facilities, for running a large DM simulation in a Λ cold DM (ΛCDM) cosmology. The cosmological parameters used were $\sigma_8 = 0.8$, $n_{\rm s} = 0.96$, $\Omega_\Lambda = 0.74$ and $\Omega_{\rm m} = 0.26$. The initial conditions were generated with the Eisenstein and Hu power spectrum at an initial redshift of $z = 159$. Table 1 lists the basic simulation parameters: the size of the box $L_{\rm box}$, the number of particles $N_{\rm part}$, the mass of a DM particle $m_{\rm DM}$ and the softening length ϵ. Note for reference, our simulation volume is roughly half that of the Millennium Simulation (Springel et al. 2005), but our mass resolution is about a factor of 3 better.

The frequency and redshift widths corresponding to $L_{\rm box} = 400\,h^{-1}$ Mpc at $z = 1$ are $\Delta\nu_{\rm box} = 75.8$ MHz and $\Delta z_{\rm box} = 0.239$. The high resolution and large volume of our simulation enable us to resolve the smallest groups expected to host H I, as well as to look for effects of cosmic variance on observables like the H I mass function. Furthermore, we are able to resolve subhaloes in the larger haloes. In fact, we will use the distribution of subhaloes in redshift space to make predictions on how these subhaloes affect the total H I signal.

We use the SUBFIND code (Springel et al. 2001) to find the subhalo catalogue and to measure properties like central coordinate, peculiar velocity, bound mass, maximum circular velocity and velocity dispersion for every subhalo. Groups of particles are retained as a subhalo when they have at least 20 bound particles, which corresponds to a minimum group mass of $M_{\rm halo} = 6.3 \times 10^9\,h^{-1}\,{\rm M}_\odot$. This mass is slightly larger than the mass of the smallest halo which is capable to host H I, as discussed in Section 3. The largest subhalo in a friends of friends (FOF) halo is generally characterized by SUBFIND as the central halo, and the other bound structures as satellites. Since the central halo contains most of the mass of the halo, we will loosely refer to it as the halo, and to the smaller ones in its vicinity as subhaloes or satellites, where appropriate.

3 MODELLING THE H I DISTRIBUTION

Our knowledge of the H I distribution in the Universe out to $z \simeq 5$ is derived mainly from quasi-stellar object absorption spectra, where the gas absorbs in the Lyman α transition of the hydrogen atom. We know from observations that much of the intergalactic medium is highly ionized and does not contain a significant amount of neutral hydrogen. Instead, most of the neutral hydrogen resides in relatively

rare DLAs (Wolfe, Gawiser & Prochaska 2005). DLAs and other high column density absorption features are believed to arise due to gas within galaxies (Haehnelt, Steinmetz & Rauch 2000; Gardner et al. 2001). It is possible to make an estimate of the total neutral hydrogen content in DLAs and study the evolution of the total neutral hydrogen content of the Universe (Storrie-Lombardi, McMahon & Irwin 1996; Rao & Turnshek 2000; Péroux et al. 2005; Prochaska, Herbert-Fort & Wolfe 2005; Rao, Turnshek & Nestor 2006; Noterdaeme et al. 2009). Interestingly, these observations suggest that the neutral hydrogen content of the Universe is almost constant in the redshift range $0.5 \leq z \leq 5$, with a density parameter of $\Omega_{\rm H\,I} \simeq 0.001$.

At low redshifts, the H I content can be estimated more directly through emission in the hyperfine transition. Observations of the HIPASS[3] galaxies (Zwaan et al. 2005) in the local universe indicate a much lower neutral hydrogen content [$\Omega_{\rm H\,I}(z=0) \simeq 4.6 \times 10^{-4}$] than seen at $z \geq 1$. These authors observed H I in emission of $\simeq 4000$ galaxies in the local Universe to estimate the H I mass function. At higher redshifts, observations in the DEEP2 survey (Gerke et al. 2007) indicate that the fraction $f_{\rm b}$ of blue galaxies (generally associated with late-type gas-rich galaxies with significant star formation activity) in groups is much higher at redshifts $0.75 \leq z \leq 1.3$, increasing from $f_{\rm b} = 0.84$ at $z = 0.75$ to $f_{\rm b} = 0.94$ at $z = 1.3$, than what is observed in the local Universe. These observations also suggest that $f_{\rm b}$ for group and field galaxies approaches the same value by $z = 1.3$. We use these observations to motivate our model of assigning H I to DM haloes at $z = 1$.

Here we use the observations of H I in emission at $z = 0$ (Zwaan et al. 2005) to match the H I mass function to the DM halo mass function. We remind the reader that the halo catalogue consists of both centrals and satellites. The Zwaan et al. (2005) H I mass function is given in a Schechter-like form:

$$\Theta\left(M_{\rm H\,I}\right) = \theta^* \left(\frac{M_{\rm H\,I}}{M^*_{\rm H\,I}}\right)^{-\alpha} \exp\left(-\frac{M_{\rm H\,I}}{M^*_{\rm H\,I}}\right), \quad (1)$$

where $\theta^* = 6 \times 10^{-3}\, h_{75}^3\, {\rm Mpc}^{-3}$ is the normalization factor, $\log(M^*_{\rm H\,I}/{\rm M}_\odot) = 9.8\, h_{75}^{-2}$ is the characteristic mass that defines the kink in the function, and $\alpha = 1.37$ is the slope at the low-mass end. $h_{75} = 0.75$ is the dimensionless Hubble constant. We vary the other models around it.

Marín et al. (2010) took a similar approach to compute the H I bias out to redshifts $z = 4$. They also incorporated the fraction of blue galaxies in the local Universe, which is much smaller than what is seen at $z = 1$ in their model. For this study we take this fraction to be unity. Additionally, we use some input from semi-analytical models and simulations of high-redshift DLAs to motivate our model. Semi-analytical models (Power et al. 2010; Kim et al. 2011) suggest that the shape of the H I mass function does not evolve considerably, but shifts toward the high-mass end with redshift, assuming a constant molecular to atomic hydrogen ratio, H_2/H I; though these results may change if this ratio is not a constant (Obreschkow & Rawlings 2009a; Obreschkow et al. 2009a,b; Obreschkow & Rawlings 2009b). This shift may be due to the higher H I content at high redshift, e.g. $\Omega_{\rm H\,I}(z=1) \simeq 10^{-3}$ as compared to $\Omega_{\rm H\,I}(z=0) \simeq 4.6 \times 10^{-4}$. However, these models do not match the low end of the Zwaan et al. mass function, due to finite resolution effects of their merger trees.

Hydrodynamic simulations of DLAs at $z = 3$ by Pontzen et al. (2008) yield a mapping from halo mass to H I mass, which can be described by

$$M_{\rm H\,I} \propto \frac{\left(M_{\rm halo}\right)^m}{1 + \left(\frac{M_{\rm halo}}{M_{\rm min}}\right)^n + \left(\frac{M_{\rm halo}}{M_{\rm max}}\right)^p}. \quad (2)$$

These authors found that there is a tight monotonic relation between the virial mass and the H I mass of haloes with some scatter. They further found that the $M_{\rm H\,I}$–$M_{\rm halo}$ relation has a break at $M_{\rm halo}/{\rm M}_\odot \simeq 10^{10.5}$, suppressing H I in haloes larger than this mass and a still stronger suppression in haloes with mass $M_{\rm halo}/{\rm M}_\odot > 10^{11.0}$. Furthermore, haloes with masses as low as $M_{\rm halo}/{\rm M}_\odot \simeq 10^{9.0}$ (or circular velocity at $z = 3$ of $v_{\rm circ} \simeq 30\,{\rm km\,s^{-1}}$) are able to host a significant amount of H I. The gas in these haloes is able to self-shield from the photoionizing UV background and maintain a significant amount of H I even though the amount of gas is insufficient for sustaining star formation.

The form of equation (2) contains two mass parameters, $M_{\rm min}$ and $M_{\rm max}$, for the three regimes in the $M_{\rm H\,I}$–$M_{\rm halo}$ relation of Pontzen et al. (2008). Based on their simulations, we choose the cut-off mass for haloes not hosting any H I to be $M \simeq 10^{9.0}\, h^{-1}\, {\rm M}_\odot$ or $v_{\rm circ} \simeq 30\,{\rm km\,s^{-1}}$ at $z = 3$. We use the scaling relation:

$$M_{\rm vir} \simeq 10^{10} {\rm M}_\odot \left(\frac{v_{\rm circ}}{60\,{\rm km\,s^{-1}}}\right)^3 \left(\frac{1+z}{4}\right)^{-3/2} \quad (3)$$

with $v_{\rm circ} = 30\,{\rm km\,s^{-1}}$ to determine the cut-off mass of haloes which do not host significant H I. This translates to $M^{\rm halo}_{\rm cut-off}/{\rm M}_\odot = 10^{9.55}$ at $z = 1$.

Table 2 summarizes all the parameters for our three models for the H I distribution over haloes. Our reference model (model 1) matches the Zwaan et al. mass function but is renormalized to $\Omega_{\rm H\,I}(z = 1) = 10^{-3}$. We also consider two alternative models around the reference model. In model 2, we allow a larger fraction of H I in large mass haloes and suppress H I in lower mass haloes. The third model is one in which the H I content in high-mass haloes is suppressed and the H I is redistributed to lower mass haloes. Given our lack of knowledge about how H I populates DM haloes, these three models should encompass a reasonable range of possibilities. All models are normalized to the fiducial value of $\Omega_{\rm H\,I} = 10^{-3}$. The form of the mapping from DM halo mass, $M_{\rm halo}$, to H I mass, $M_{\rm H\,I}$, is given in equation (2), which is a more generalized form of the mapping considered by Wyithe & Brown (2010). Note that the ratio of the indices m and p determines the H I content of haloes with mass $M_{\rm halo} > M_{\rm max}$. In models 2 and 3, $m/p = 1$, which means that the H I content in haloes larger than $M_{\rm max}$ approaches a constant. On the other hand, the value $m/p < 1$ for model 3 suppresses H I in larger haloes.

Table 2. Model parameters: mapping of H I mass to halo (centrals and satellites) mass for the three models that we consider. See equation (2) for the functional form of the mapping from H I mass to halo mass.

Model	$M_{\rm min}$ ($10^{10}\,h^{-1}\,{\rm M}_\odot$)	$M_{\rm max}$ ($10^{10}\,h^{-1}\,{\rm M}_\odot$)	m	n	p
1	12	143	1.8	1.36	1.8
2	12	143	2.0	1.36	2.0
3	5	143	1.6	1.15	1.7

The model mass functions for all the three models are shown in the left-hand panel of Fig. 1. The fiducial mass function (solid line) is the one whose shape matches that of the Zwaan et. al mass function, but is normalized to $\Omega_{\rm H\,I} = 10^{-3}$. The mass function of model 2 (dashed line) has comparatively more H I in larger haloes

[3] H I Parkes All Sky Survey: http://www.parkes.atnf.csiro.au.

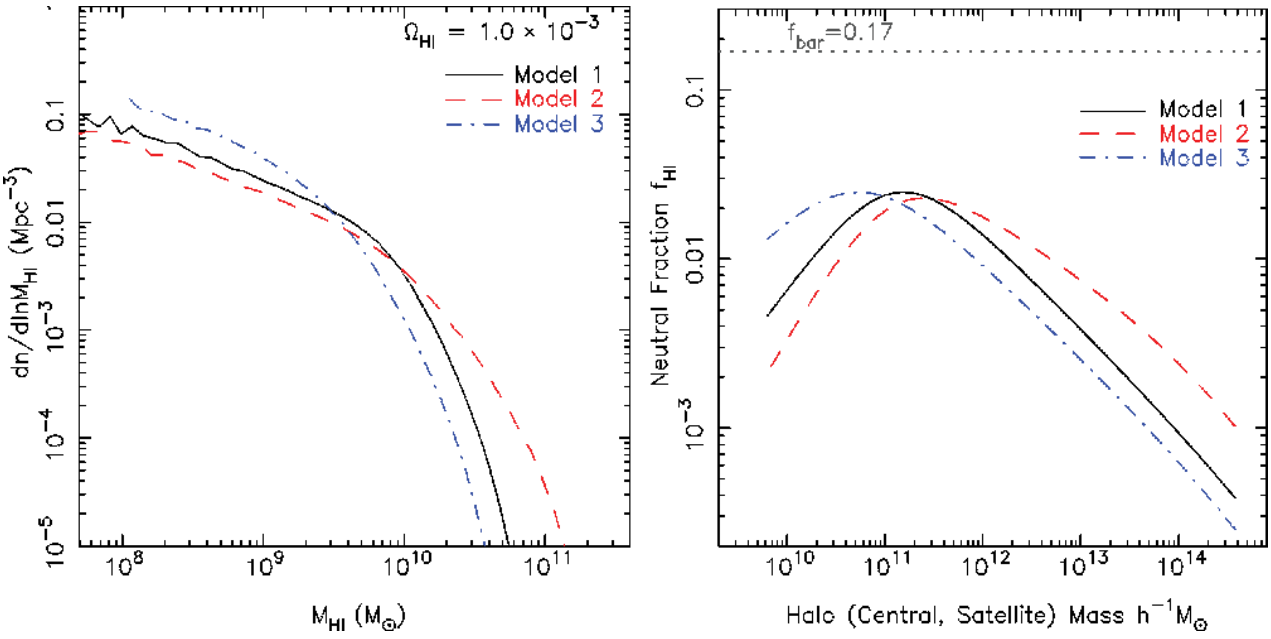

Figure 1. Left: the mass function for the three models that we consider. Model 1 (solid line) is the Zwaan et al. (2005) mass function but normalized to $\Omega_{\rm H\,I} = 10^{-3}$. Models 2 (dashed) and 3 (dot–dashed) are variations around model 1 (see Table 2 and equation (2) for details of the model parameters). Right: the neutral mass fraction $f_{\rm H\,I} = M_{\rm H\,I}/M_{\rm halo}$ as a function of halo mass for the three models. The (dotted) horizontal line is the baryon mass fraction.

while the H I in smaller haloes is suppressed. On the other hand, the mass function of model 3 (dot–dashed line) suppresses H I in larger haloes, with the H I being redistributed to lower mass haloes.

In the right-hand panel of Fig. 1, we plot the mass fraction of H I ($f_{\rm H\,I} = M_{\rm H\,I}/M_{\rm halo}$) as a function of the mass of the host halo. In all three cases, the H I fraction is peaked around haloes of mass in the range $6 \times 10^{10}\,h^{-1}\,{\rm M}_\odot < M_{\rm halo} < 2 \times 10^{11}\,h^{-1}\,{\rm M}_\odot$, and the peak value is 14 per cent of the baryon mass fraction $f_{\rm bar} = \Omega_{\rm b}/\Omega_{\rm m} = 0.17$. Lower and higher mass haloes have a suppressed H I fraction, which is due to the ratio of slopes (m/n) and (m/p) being smaller or equal to unity in equation (2). The dependence of the H I mass on halo mass is again reflected by the three models. At lower halo masses, model 3 has a higher H I fraction followed by model 1 and model 2, however, at the higher mass end the situation is reversed. This is also illustrated in Fig. 2, where we show the distribution of DM particles at $z = 1$ in a thin slice through our simulation enclosing the largest halo. The bottom panels zoom-in to a region of dimension $50 \times 50 \times 4\,(h^{-1}{\rm Mpc})^3$ centred on the largest halo and showing the H I fraction $f_{\rm H\,I}$ for haloes only, for the three models (left to right). As discussed earlier, the smaller mass haloes in model 3 have a higher neutral fraction in comparison to the other two models. In all models the largest haloes have a smaller neutral fraction, with model 2 dominating over the other two models.

Before proceeding, it is worthwhile to point out the advantages of using a numerical N-body simulation over a halo model based approach. In the latter, properties like halo (and subhalo) abundances, halo profiles, velocity dispersions and the halo-to-halo scatter are typically calibrated from simulations such as ours (even so often based on much smaller ones). Once appropriate fitting functions are determined, they can be used to predict the signal to a certain accuracy. However, the approach cannot be used to construct a mock map with which the efficiency of signal extracting can be studied. The clustered distribution of haloes in a volume is crucial for properly describing the signal. Haloes often occupy common pixels in a map and may add in various combinations to the total signal of a given pixel. The noise in a pixel is a fixed random value irrespective of how many haloes contribute to the signal in that pixel. Techniques for extracting the signal from a map need to be explored when presenting results for its detectability with instruments. A halo model is generally not able to account for these effects accurately and as a result tends to overpredict the significance of detection. This issue will become clearer when we discuss how the signal is extracted from a mock map for the noise levels that we consider, in Sections 4 and 5.

3.1 A common field of view for DEEP2 and the GMRT

In this section, we describe our fiducial choices for volume and haloes based on the specifications of the DEEP2 survey and the GMRT. The GMRT is a radio interferometer, consisting of 30 45-m diameter antennas spread over 25 km. Half of the antennas are spread over a central compact array of diameter 1 km, and the remaining half are spread on three arms of length 14 km in a Y-shaped distribution. The longest baseline is 26 km and the shortest 100 m. The GMRT operates on five central frequencies (151, 235, 325, 610, 1420 MHz). For this work our focus is on the 610-MHz frequency which corresponds to a redshift of $z = 1.3$ for the 21-cm line. The operational redshift at this frequency is $1.18 \leq z \leq 1.44$. The angular resolution (corresponding to the largest effective baseline) is 5 arcsec, this translates to a comoving scale of $d = 67\,h^{-1}$ kpc. The system temperature is $T_{\rm sys} = 102$ K and the antenna sensitivity $K = 0.32$. The GMRT has a full bandwidth of 32 MHz over 256 channels.

The DEEP2 survey is a redshift survey with spectra for ≃40 000 galaxies in the redshift range $0.7 \leq z \leq 1.4$. The survey covers four strips of dimensions $0.^\circ5 \times 2^\circ$ of the sky which corresponds to $20 \times 80\,h^{-1}$ Mpc (comoving) at $z = 1$. The total comoving volume of DEEP2 is $6 \times 10^6 (h^{-1}\,{\rm Mpc})^3$. The spectral resolution of DEEP2 is ≃68 km s^{-1}, and targets were pre-selected to a limiting magnitude of $R = 24.1$. The DEEP2 spectroscopically targets ≃60 per cent of

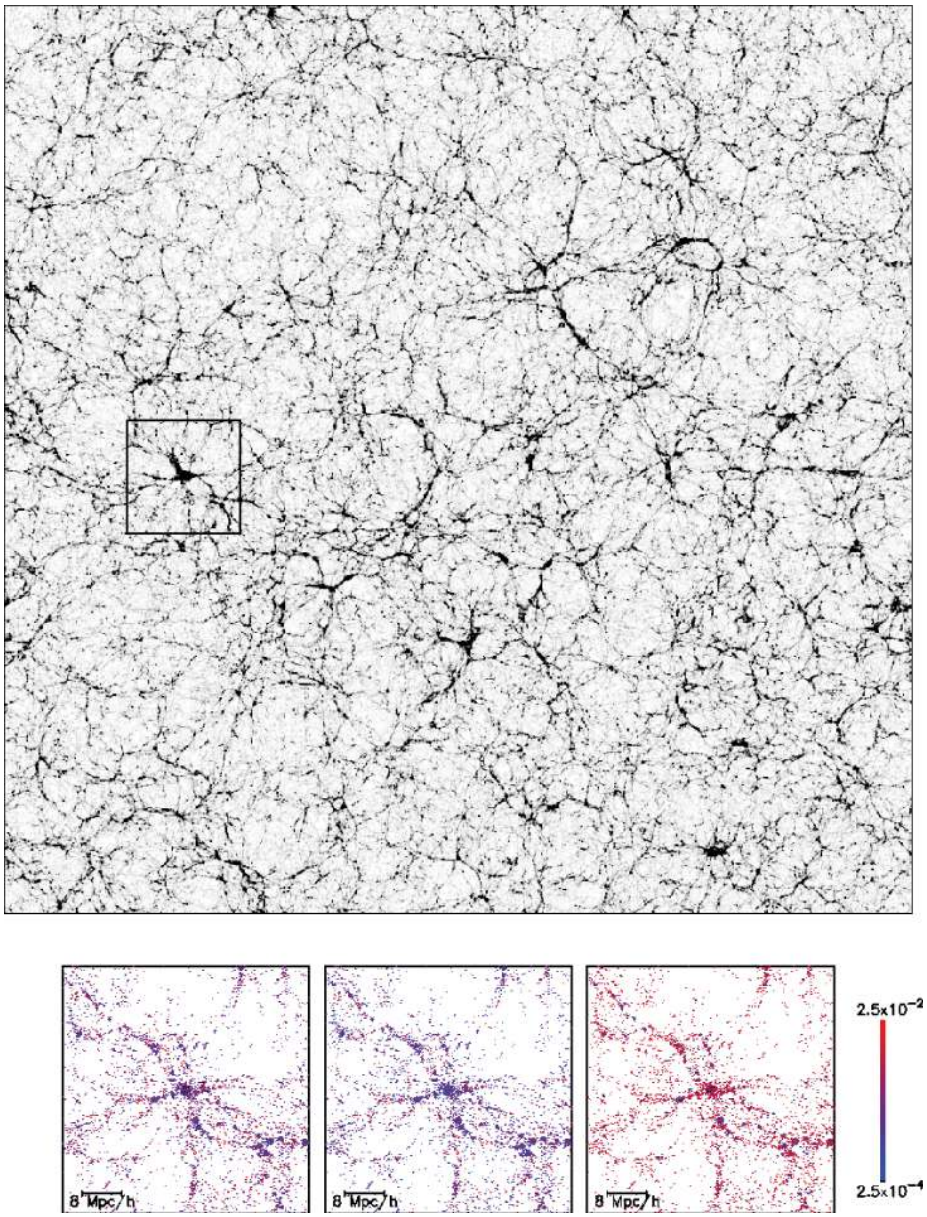

Figure 2. Top: a thin slice of our simulation enclosing the largest halo (square box), showing the distribution of DM particles. Bottom: a zoom-in for a region of dimension $50 \times 50 \times 4(h^{-1}\,\mathrm{Mpc})^3$ centred on the largest halo in our simulation, showing the haloes which host H I, colour-coded with the neutral fraction $f_{\mathrm{H\,I}}$. The panels from left to right are for the three models.

the objects that pass the apparent magnitude limit. We hence take the completeness of DEEP2 to be $\simeq$60 per cent.

The overlapping redshift range between DEEP2 and GMRT is $1.18 \leq z \leq 1.4$, which corresponds to $288\,h^{-1}$ Mpc in depth, or nearly a quarter of the DEEP2 volume. Our H I model is at the fixed redshift $z = 1$ of the simulation output, and not exactly matched to the redshift range of the GMRT, which would require a light cone simulation. Our results should however be a good approximation to redshift averaged quantities such as the mass function. We choose our analysis volume to be of dimension $50 \times 80 \times 400\,(h^{-1}\,\mathrm{Mpc})^3$, which is a quarter of the DEEP2 volume. In order to match the required number density of galaxies in DEEP2 (and account for its finite completeness), we choose a minimum threshold mass of $M > 10^{11.4}\,h^{-1}\,\mathrm{M}_{\odot}$. Conroy et al. (2007) compute the mass-to-light (B magnitude) ratios for haloes in the DEEP2 survey for $M > 10^{12.0}\,h^{-1}\,\mathrm{M}_{\odot}$. These results can in principle be used to relate the mass of the halo to its luminosity.[4] However, one will need to extrapolate them to lower masses such as considered here in order to get an estimate of the luminosities of haloes with $10^{12.0}\,h^{-1}\,\mathrm{M}_{\odot} > M > 10^{11.4}\,h^{-1}\,\mathrm{M}_{\odot}$. Owing to the large errors in these estimates of mass-to-light ratio, we will stick to a mass cut rather than a luminosity cut for selecting galaxies. Above this threshold mass, there are 16 388 haloes in the subvolume which we identify as galaxies. We also adopt two larger threshold masses for testing our detection strategy; these are $M > 10^{12.0}\,h^{-1}\,\mathrm{M}_{\odot}$ and $M > 10^{12.5}\,h^{-1}\,\mathrm{M}_{\odot}$. For these mass cuts there are 3835 and 1031 haloes, respectively.

[4] We find that a halo of mass $M = 10^{12.0}\,h^{-1}\,\mathrm{M}_{\odot}$ at $z = 1.0$ has an apparent R-magnitude of $m_{\mathrm{R}} = 23.2 \pm 0.3$ from the results of Conroy et al. (2007).

We wish to point out that in the overlapping volume that we consider here there are ∼1300 galaxies per DEEP2 field or ∼5200 galaxies in total. The number of objects in the lowest mass bin of $10^{12.0}\,h^{-1}\,\mathrm{M}_\odot > M > 10^{11.4}\,h^{-1}\,\mathrm{M}_\odot$ is more strongly affected by selection effects. Observational results need to take into account the effect of the selection function when comparing theoretical results presented here.

The primary beam of the GMRT corresponds to around 50 Mpc at $z \sim 1.3$. However, sensitivity drops rapidly from the centre of the beam. This means that only roughly half of the primary beam might be usable to attain maximum sensitivity. We note that the selection function of DEEP2 is falling at $z > 1.3$. If observers were to target the four DEEP2 fields up to $z \sim 1.3$, then one would require 12-16 GMRT pointings (or 300-400 h in total for a single pointing of 24 h). This number would double if one were to target the entire field of DEEP2 under consideration.

3.2 Comparison with observations

Recently, Chang et al. (2010) reported the first detection of H I in emission from $z \simeq 0.8$. They cross-correlated the optical galaxy density field (from DEEP2) with the signal from the redshifted H I line using the Green Bank Telescope (GBT) to obtain a 4σ detection. At $z \simeq 0.8$, the GBT's angular resolution corresponds to a full width at half-maximum (FWHM) of $9\,h^{-1}$ Mpc (comoving), but the frequency resolution $\simeq 2\,h^{-1}$ Mpc is much finer. Owing to the much poorer angular resolution, Chang et al. (2010) computed the cross-correlation along the line-of-sight direction.

To make a detailed comparison with these observational results, we convolve our simulation box with the angular and frequency resolution to match the analysis of Chang et al. (2010). We also follow Chang et al. (2010) in assuming pixels of size $(2\,h^{-1}\,\mathrm{Mpc})^3$. Note that our density field is at $z \simeq 1$, whereas the observations are at $z \simeq 0.8$. This should not pose a serious problem while comparing results, since the only quantity which changes is the mass function of haloes and this variation can be absorbed within the models that we consider. We first compute the fluctuating component of both the H I and the galaxy density field on a pixel of size $(2\ h^{-1}\ \mathrm{Mpc})^3$. We then convolve these two fields with GBT's point spread function, modelled as a Gaussian with FWHM of $9\ h^{-1}$ Mpc in the transverse direction and a top-hat of width $2\ h^{-1}$ Mpc in the redshift direction.

In order to mimic the optical-H I observations, we only assign haloes with $M > 10^{11.4}\,h^{-1}\,\mathrm{M}_\odot$ in the volume while constructing the galaxy density field. We do not use such a threshold when constructing the H I density field. The cross-correlation as a function of relative displacement, r_z, along the line-of-sight direction, can be expressed as (Chang et al. 2010)

$$\xi_{\mathrm{HI,opt}}(r_z) = \langle \Delta T_\mathrm{b}(d + r_z)\delta_\mathrm{opt}(d)\rangle$$
$$= 284\,\mu\mathrm{K}\langle\delta_{\mathrm{H\,I}}(d + r_z)\delta_\mathrm{opt}(d)\rangle \left(\frac{\Omega_{\mathrm{H\,I}}}{10^{-3}}\right)\left(\frac{h}{0.72}\right)$$
$$\times \left(\frac{\Omega_\mathrm{m} + (1+z)^{-3}\Omega_\Lambda}{0.37}\right)^{-0.5}\left(\frac{1+z}{1.8}\right)^{0.5}. \qquad (4)$$

Here $T_\mathrm{b} = 284\ \mu$K is the 21-cm mean sky brightness temperature, δ_opt is the optical density field and $\delta_{\mathrm{H\,I}}$ is the neutral hydrogen density field. They are related by $\delta_{\mathrm{H\,I}} = br\delta_\mathrm{opt}$, where $b = \langle\delta^2_{\mathrm{H\,I}}\rangle^{1/2}/\langle\delta^2_\mathrm{opt}\rangle^{1/2}$ is the bias and $r = \langle\delta_{\mathrm{H\,I}}\delta_\mathrm{opt}\rangle/(\langle\delta^2_{\mathrm{H\,I}}\rangle\langle\delta^2_\mathrm{opt}\rangle)^{1/2}$ is the stochasticity. By construction $|r| \leq 1$. Inserting this into equation (4), one can see that the amplitude of the cross-correlation function determines the degenerate combination $br\Omega_{\mathrm{H\,I}}$. Chang et al. (2010) put a constraint on this combination of parameters, obtaining $br\Omega_{\mathrm{H\,I}} = (5.5 \pm 1.5) \times 10^{-4}$. In our simulation we can break this degeneracy. Note that r and b are both dimensionless and do not depend on $\Omega_{\mathrm{H\,I}}$. We find for the three models, $b = (0.578, 0.641, 0.538)$ and $r = (0.923, 0.945, 0.916)$, respectively. Using the product rb we put a constraint on $\Omega_{\mathrm{H\,I}}$ for all the three models, $\Omega_{\mathrm{H\,I}} = (1.03 \pm 0.28, 0.95 \pm 0.26, 1.12 \pm 0.30) \times 10^{-3}$. These values are consistent with the value of $\Omega_{\mathrm{H\,I}} = 10^{-3}$ taken in our study.

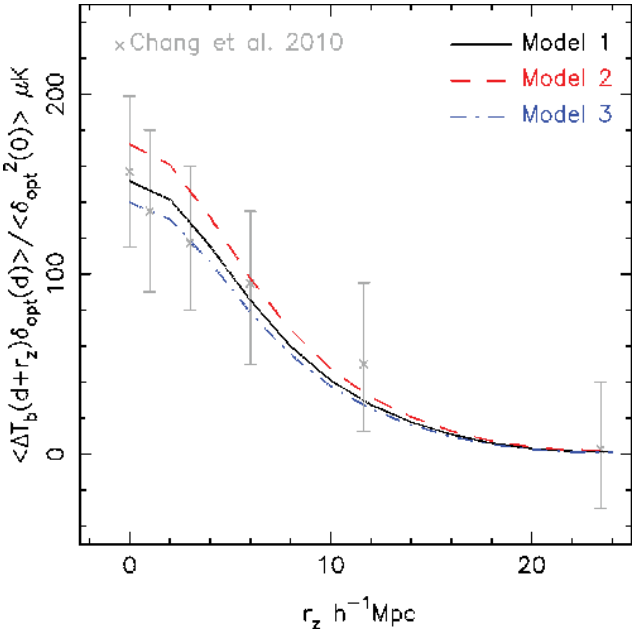

Figure 3. Normalized cross-correlation function of the DEEP2 optical galaxy density field and the H I intensity field along the line-of-sight direction (Chang et al. 2010) (data points), and the models 1 (solid line), 2 (dashed line) and 3 (dot–dashed line) that we consider. Note that the cross-correlation function is normalized by the zero-lag autocorrelation function $\delta^2_\mathrm{opt}(0)$ of the DEEP2 optical galaxy density field.

Chang et al. (2010) also computed the cross-correlation along the line-of-sight direction and normalized it by $\langle\delta^2_\mathrm{opt}(0)\rangle$. We plot the normalized cross-correlation function in Fig. 3 for the three models (solid, dashed and dot–dashed) and compare with the observations of Chang et al. (2010). We find that all the three models are consistent with the observations. Note that model 2 is the most biased of the three models, followed by models 1 and 3. This is expected since the largest haloes have a considerably larger H I fraction in model 2, and the largest haloes cluster more strongly at smaller scales. A suppression of H I in the largest haloes will translate to a lower small-scale bias. The large-scale bias is further discussed in the following section.

3.3 Finite volume effects on $\Omega_{\mathrm{H\,I}}$

In Fig. 4, we look at finite volume effects in the estimation of $\Omega_{\mathrm{H\,I}}$. The size of the subvolume is chosen so as to match the overlapping fields of DEEP2 and the GMRT. In our full simulation volume we have 40 such subvolumes. We look at the variations in H I mass in a subvolume with respect to the average H I mass in the entire volume for the three models. These variations are shown for all three models in Fig. 4 with the same line styles as in Fig. 1. We also plot the variation in $\Omega^\mathrm{halo}_\mathrm{DM}$ (dotted line). The rms fluctuation in $\Omega_{\mathrm{H\,I}}$ for the three models is $\simeq$6.8, 7.6 and 6.2 per cent respectively, whereas the rms fluctuation in $\Omega^\mathrm{halo}_\mathrm{DM}$ is 8.9 per cent. Given that the neutral mass fraction is not uniform but rather peaked around halo masses

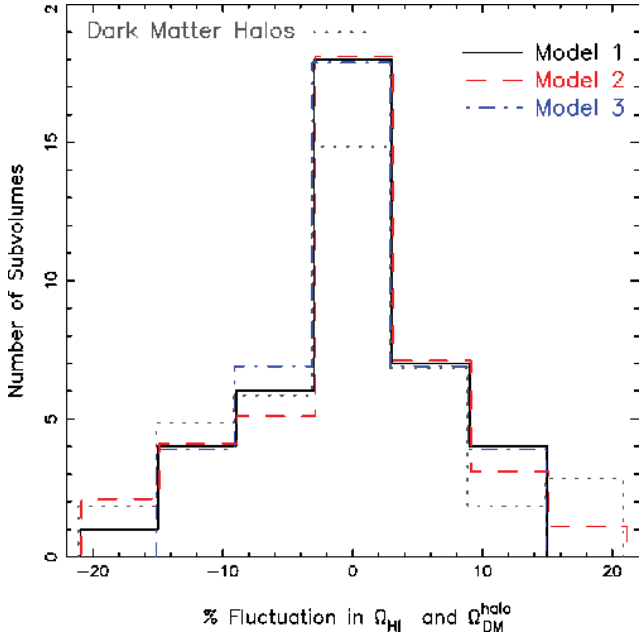

Figure 4. Fluctuations in $\Omega_{\rm H\,I}$ for the three models for a subvolume of dimension $50 \times 80 \times 400\,(h^{-1}\,{\rm Mpc})^3$ that we consider. We have a total of 40 such subvolumes. The subvolumes considered for computing fluctuations in $\Omega_{\rm H\,I}$ were the same for all three models. The 1σ fluctuations for the three models are 6.8, 7.6 and 6.2 per cent respectively, for DM this value is 8.9 per cent.

in the range of $6 \times 10^{10}\,h^{-1}\,{\rm M}_\odot < M_{\rm halo} < 2 \times 10^{11}\,h^{-1}\,{\rm M}_\odot$ and suppressed for larger and smaller masses (Fig. 1), the DM haloes are more strongly biased than H I. This is consistent with Bagla et al. (2010) who showed that the large-scale H I bias increases with a higher neutral fraction in larger haloes. Indeed we see that the fluctuation in $\Omega_{\rm H\,I}$ in model 2, which has more H I in larger haloes, is closer to that of DM haloes than the other two models, with model 3 having the least fluctuations. The final volume for our analysis is picked based on the consideration that it should have the smallest fluctuations in H I mass with respect to the mean for the reference model 1.

4 THE 21-cm EMISSION SIGNAL

Since the 21-cm line has much larger wavelength than any optical line, the resolution of a radio image is generally much poorer compared to an image made in the optical. Especially at high redshift, a typical radio observation will be looking at most at a few coarse pixels enclosing the target object rather than resolving it with a large number of finer pixels.

In order to create a simulated radio data cube we create a mesh out of the box with each pixel corresponding to an angular width of $125\,h^{-1}$ kpc (comoving), and frequency depth of 125 kHz (this is the width per channel of the GMRT for a single pointing and matches the spectral resolution of DEEP2). The angular resolution is chosen to match that corresponding to the largest baseline of the GMRT. The H I mass in every pixel is computed by integrating the H I mass profiles of haloes in the pixels they cover, where a Gaussian profile with a width given by the velocity dispersion of the halo is assumed in redshift or frequency space. Since observations are done in redshift space, we have added the line-of-sight component of the peculiar velocity of the halo to its real space line-of-sight z-coordinate to obtain its redshift space coordinate.

The stacking of haloes is done in the following manner. Haloes are first sorted according to their mass. We then identify the central pixel of the halo corresponding to its redshift and its centre in the image plane. Given the location of haloes as well as their angular and frequency widths, we first select pixels along a line of sight (in frequency) and passing through the central pixel. Stacking is done on the central or zero-reference frequency. For every halo i the frequency range stacked is $\pm(4 \times \Delta\nu_i)$ around the halo centre. Once stacked pixels are flagged so as to avoid double counting. After this is done for every target halo, we repeat this procedure for lines of sight not passing through the centre but neighbouring pixels in cases where the halo is spread across more pixels. Finally, the search for pixels in frequency space is increased in order to stack the wings of the signal.

In case two target haloes whose centres lie within the same line of sight are overlapping within $\pm(4 \times \Delta\nu)$ of each other, parts of the smaller target halo may appear on the wings of the stacked spectra. However, the order of stacking ensures that two haloes along the same line of sight are stacked in an optimal manner. If we had chosen to stack around the first halo with the entire frequency range (corresponding to the box), then the second halo would appear on the wing of the first halo. We have checked that with a frequency width of the pixel finer than 64 kHz we are able to recover the signal reasonably well with this method, similar to what one would get from just stacking analytically (as in a halo model) the flux, S_ν, of selected haloes of mass $M_{\rm H\,I}$ located at a luminosity distance $D_{\rm L}(z)$ with a line profile $\phi(\nu)$:

$$S_\nu = \frac{3}{4}\frac{A_{12} M_{\rm H\,I} h\nu}{m_{\rm H}} \frac{1+z}{4\pi D_{\rm L}(z)^2}\phi(\Delta\nu). \quad (5)$$

Here ν is the redshifted frequency $\nu = \nu_0/(1+z)$, A_{12} is the Einstein coefficient for spontaneous transition from the upper to the lower level, h is Planck's constant and $m_{\rm H}$ is the mass of the hydrogen atom. $\phi(\Delta\nu)$ is the line profile which we take to be a Gaussian of width $\Delta\nu = \nu(\Delta v/c)$, with Δv being the velocity dispersion of the halo.

Uncertainties in the redshifts of the DEEP2 galaxies can dilute the stacked 21-cm signal. Repeated observations of the DEEP2 galaxies find that the rms redshift errors are $\Delta z_{\rm err} < 35\,{\rm km\,s^{-1}}$ (Coil et al. 2008). We find that when we include an error in redshift of rms $\Delta z_{\rm err} = 35\,{\rm km\,s^{-1}}$ the peak of the stacked signal is diluted by less than 3 per cent. As will be seen in our analysis the uncertainties in determining the global H I signal are dominated by the system noise and cosmic variance. We therefore neglect the effect of the redshift errors for the rest of our analysis.

4.1 Effect of subhaloes on the H I signal

The signal computed from a halo catalogue is different to that extracted from a map. The H I content in the pixels enclosing a target object is typically greater than the H I mass of the object since lower mass haloes as well as interlopers (due to peculiar velocities) add to the pixel with their own H I mass, thereby increasing the signal. This effect is larger in redshift space. In Fig. 5 we look at this effect for all the models and for the three mass cuts of $M \geq 10^{11.4}\,h^{-1}\,{\rm M}_\odot$ (left), $M \geq 10^{12.0}\,h^{-1}\,{\rm M}_\odot$ (centre) and $M \geq 10^{12.5}\,h^{-1}\,{\rm M}_\odot$ (right). The average signal (in μJy) per halo is plotted as a function of frequency, the zero-frequency marks the central frequency where we have stacked spectra of individual haloes. We compare the signal a mock observation would measure (dashed line) when targeting objects with masses above a threshold mass, with the theoretical or modelled expectation (solid line). The modelled

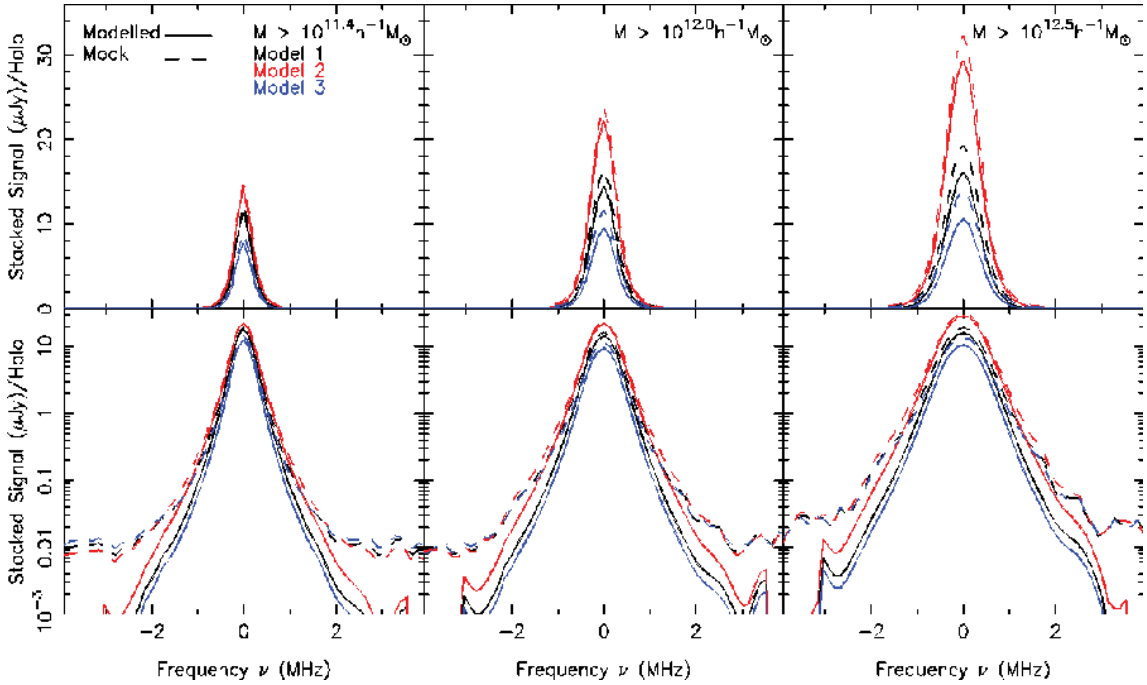

Figure 5. The modelled H I emission signal per halo (solid) and the mock signal (dashed), recovered from the radio data cube by stacking, for the three mass cuts $M \geq 10^{11.4}\,h^{-1}\,\mathrm{M}_{\odot}$ (left), $M \geq 10^{12.0}\,h^{-1}\,\mathrm{M}_{\odot}$ (centre) and $M \geq 10^{12.5}\,h^{-1}\,\mathrm{M}_{\odot}$ (right). The excess signal in the mock data is due to haloes and subhaloes below the mass thresholds, which were not identified for stacking. The second row is the same as the first but replotted on a logarithmic y-axis to better illustrate the broader wings due to subhaloes.

signal was constructed by assigning only those haloes above the mass cuts in the data cube. Haloes below the threshold mass were not assigned to the data cube. In the mock observation, all haloes were assigned to the radio data cube and the spectra were stacked for haloes above the threshold mass. The contribution of lower mass haloes can be seen in Fig. 5 where the plots in the second row are the same as those in the first row, but replotted on log-y scale. This is done so as to better illustrate the difference in the wings of the stacked signal, with and without the subhaloes. The average signal decreases with decreasing mass cut since lower mass haloes have on average a lower peak signal. There is also scatter in the relationship between halo mass (hence H I mass) and peak signal since both the velocity dispersion and the H I mass determine the shape of the signal.

In the mock spectra, we find an enhanced peak and broader wings for all the three mass cuts and models. The enhanced signal being larger for the larger mass cuts. The enhancement is as much as 31 per cent for a mass cut of $M \geq 10^{12.5}\,h^{-1}\,\mathrm{M}_{\odot}$, decreasing to 9 per cent for a mass cut of $M \geq 10^{11.4}\,h^{-1}\,\mathrm{M}_{\odot}$ in model 3 where there is relatively more H I in lower mass haloes. The numbers for model 2 are smallest where the H I mass is dominated by larger mass haloes, decreasing from 10 per cent for $M \geq 10^{12.5}\,h^{-1}\,\mathrm{M}_{\odot}$ to 4 per cent for $M \geq 10^{11.4}\,h^{-1}\,\mathrm{M}_{\odot}$. For model 1, the intermediate model, the contribution of subhaloes is 22 per cent for $M \geq 10^{12.5}\,h^{-1}\,\mathrm{M}_{\odot}$ and decreases to 7 per cent for $M \geq 10^{11.4}\,h^{-1}\,\mathrm{M}_{\odot}$.

The larger haloes have more substructure as well as interlopers in redshift space, both of which lead to an enhanced signal. To illustrate this point we pick one of the larger haloes in the data cube and compute the signal from the pixels that it covers. This is shown in Fig. 6 for the three models (left to right). This particular halo has a mass of $M = 2 \times 10^{14}\,h^{-1}\,\mathrm{M}_{\odot}$. The black solid line is the (theory) spectrum of the large halo. The blue data points are the theoretical spectra computed from equation (5) of all subhaloes within the pixels covered by the large halo, the height and error bar being the peak signal and its width. These subhaloes are below the mass threshold $M < 10^{11.4}\,h^{-1}\,\mathrm{M}_{\odot}$ and will not be identified in an optical survey. If a threshold mass of $M > 10^{11.4}\,h^{-1}\,\mathrm{M}_{\odot}$ is chosen then the contribution from this large halo to the stacked spectra is the blue solid line since the more massive subhaloes with $M > 10^{11.4}\,h^{-1}\,\mathrm{M}_{\odot}$ (red data points) will be separately picked for stacking. This excess signal from these less massive subhaloes can be as much as 50 per cent of the total signal in model 3, 13 per cent in model 2 and 35 per cent in model 1. The enhanced signal due to these undetected subhaloes is within a $2\Delta\nu$ width of the large halo. If one were to resolve all subhaloes and stack them in this case, then one would get a peak signal in excess of $\simeq$140 μJy across models; instead since these are unresolved within the pixel width and are spread across the parent halo we get a peak signal in the range of $\simeq$22–55 μJy across models. The red data points are larger haloes, also within the pixels covered by the targeted halo, which are above the minimum mass threshold and would be identified in the optical survey. If one were to target the large halo only, then we would get an even larger signal (red dot–dashed line). The effect of subhaloes will show up when we recover the cumulative H I mass from the stacked signal in a later section.

One limitation of our model is that we assign an equal amount of H I to both satellite and distinct field haloes of the same mass. It is known that gas is stripped from a halo when it merges into a larger halo. Our models hold if an equal fraction of cold gas and DM is stripped from a halo during a merger. Conroy, Wechsler & Kravtsov (2006) argue that the mass of a halo at the time of a merger, M_{infall}, is a better predictor of stellar mass (hence luminosity) than the mass of the halo, M_{obs}, when it is already a satellite. By doing an abundance matching of the luminosity function to the halo mass function with their new definition of mass for satellites, their model reproduces luminosity-dependant clustering of galaxies seen in observations.

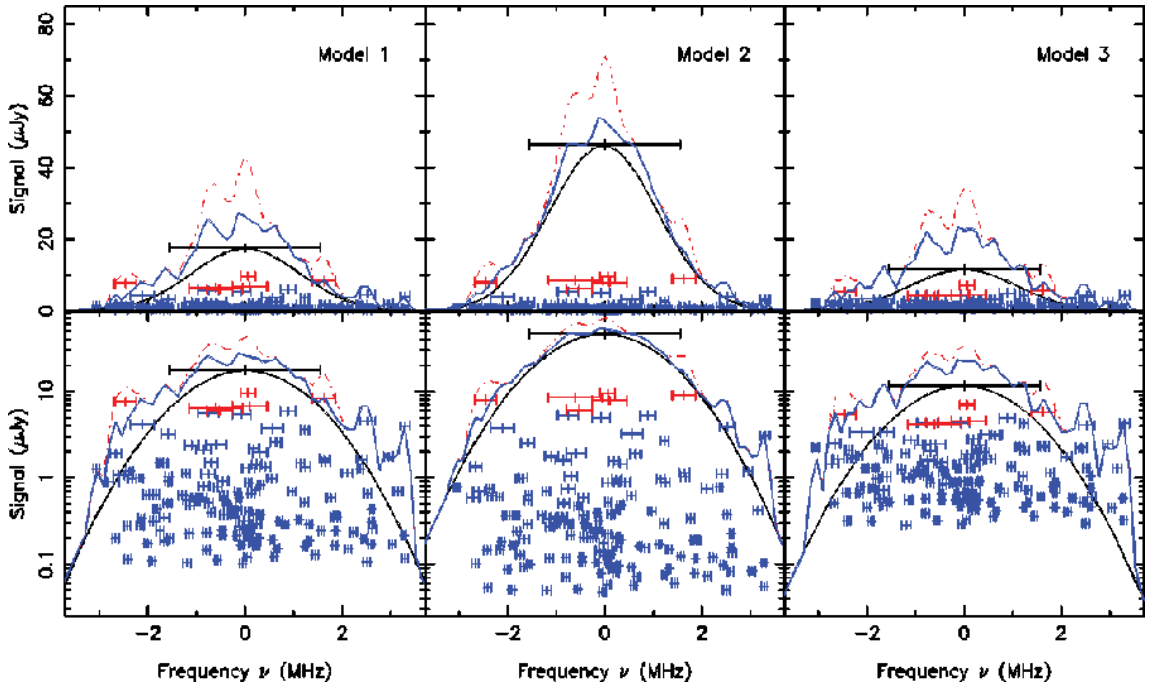

Figure 6. Contribution of subhaloes and interlopers to the H I signal of a single large halo for the three models (left to right). Height and error bars of each data point denote the peak and width of the theoretical signal of each subhalo or halo. The red data points are for subhaloes $M > 10^{11.4}\,h^{-1}\,\mathrm{M}_{\odot}$ and will be identified in an optical survey, whereas the blue data points are for subhaloes with $M < 10^{11.4}\,h^{-1}\,\mathrm{M}_{\odot}$ and will not be identified in the optical survey. If a threshold mass of $M > 10^{11.4}\,h^{-1}\,\mathrm{M}_{\odot}$ is chosen, then the contribution from this large halo to the stacked spectra is the blue solid line since the more massive subhaloes (red data points) will be separately picked for stacking. However, an observation targeting the large halo only would see an excess emission signal (red dot–dashed line) compared to the expected (modelled) signal (black solid line) of the large halo. This excess signal is from all subhaloes (red and blue data points). This particular halo has a mass of $M = 2 \times 10^{14}\,h^{-1}\,\mathrm{M}_{\odot}$. The second row is the same as the first but replotted on a logarithmic y-axis to better illustrate the broader wings due to subhaloes.

However, their new definition of mass of a satellite seems to affect results more strongly at $z = 0$ than at $z = 1$ or higher. If we assume cold gas to trace stars and be more concentrated in the centre of the halo, then based on the results of Conroy et al. (2006) at $z = 1$, our model should not be sensitive to the environment of small haloes. However, if cold gas is not concentrated in the centre of haloes and is largely stripped during a merger then our model may overpredict the contribution of undetected satellites to the total signal of a large halo.

5 RESULTS: DETECTING H I IN EMISSION IN THE DEEP2 FIELD WITH THE GMRT

We now focus our attention to detecting H I in emission in the common field of DEEP2 and the GMRT. We start with a discussion of noise in the GMRT and then proceed to recover the stacked H I emission signal by adding noise to the radio data cube.

5.1 Noise in images

The point source (or angular scales smaller than the synthesized beam of the interferometer) sensitivity, σ_{rms}, for an interferometer is given by (assuming two polarizations) (Thompson, Moran & Swenson 2001):

$$\sigma_{\mathrm{rms}} = \frac{T_{\mathrm{sys}}}{K}\frac{1}{\sqrt{\Delta\nu\Delta t}\sqrt{2\,N\,(N-1)}}, \qquad (6)$$

where K (in units of $\mathrm{K\,Jy^{-1}}$) is the antenna sensitivity, T_{sys} is the system temperature and N is the number of antennas, $\Delta\nu$ is the channel bandwidth and Δt is the integration time. The GMRT has a full bandwidth of 32 MHz with 256 channels, or 125 kHz channel^{-1} for the maximum bandwidth in a single pointing. For this bandwidth and $N = 30$, the noise per channel is $\simeq$71 μJy for 24 h of observation, where $K = 0.32$ and $T_{\mathrm{sys}} = 102$ K at the redshifts under consideration.

We need to make several other assumptions to bring the results of our simulation closer to the possible observational outcome. For our stacking approach, we need to co-add signal from sources occupying different pixels in the three-dimensional data cube. However, the noise in neighbouring pixels is not uncorrelated for a radio interferometer; only the noise in different frequency channels is uncorrelated. To take this complication into account, we assume here that the noise is uncorrelated for the spatially separated haloes. However, for all neighbouring pixels enclosing a target object at a fixed frequency we choose the same noise. To take into account this uncertainty in estimating the noise level and other complications owing to extraction of continuum point sources, etc., we assume two different noise levels: $\sigma_{\mathrm{rms}} = 420$ μJy, which is an estimate of an upper limit, or conservative, noise level on GMRT (see e.g. Lah et al. 2007, for a similar study at a neighbouring frequency), and $\sigma_{\mathrm{rms}} = 71$ μJy, which corresponds to the theoretical (optimistic) noise level computed for 24 h of observation.

Both noise levels correspond to a pixel of size $125\,h^{-1}$ kpc $\times$ $125\,h^{-1}$ kpc (comoving), which is matched to the approximate synthesized beam of the GMRT at $\nu \simeq 700$ MHz, and depth 125 kHz for 24 h of observation. To every pixel we add a Gaussian random noise with an rms of the two levels of noise that we consider.

5.2 Recovering the stacked H I emission spectra

Having added noise to the radio data cube we attempt to recover the stacked emission spectra by doing a χ^2 analysis. We model the stacked spectra by a Gaussian with three parameters:

$$S_{\rm bf} = N_{\rm bf} \exp\left[-\left(\frac{\nu - \nu_{\rm bf}}{\Delta\nu_{\rm bf}}\right)^2\right], \quad (7)$$

where $N_{\rm bf}$, $\nu_{\rm bf}$, $\Delta\nu_{\rm bf}$ are the best-fitting height, centre and width, respectively. We vary these three parameters over a large range, and the best-fitting values are obtained by minimizing χ^2. We illustrate this analysis for the fiducial model 1 in Fig. 7 for the three mass cuts (columns) discussed earlier and the two noise levels (rows) we consider. For a better illustration of the fits, we have changed the scales on the *y*-axis for the three mass cuts. Note that this is done for the mock spectra, where all subhaloes have been added to the radio data cube. In all cases, the reduced $\chi^2_{\rm red} \simeq 1$ which is not a good indicator of the quality of the fit. For the optimistic noise (top row) we are able to correctly recover the centre for all the three mass cuts. Visually the best fit (solid blue) seems to match the expected signal (black dashed) extremely well for this case, but note that noise has not been included here. The red line is the mock spectra where noise has been added. For the case of the conservative noise, this is true for a mass cut of $M > 10^{11.4}\,h^{-1}\,{\rm M}_\odot$ where we are able to recover the centre at the zero-reference frequency. For a mass cut of $M > 10^{12.0}\,h^{-1}\,{\rm M}_\odot$ the best-fitting centre is not the zero centre but slightly shifted to the left at $\nu_{\rm bf} = 25$ kHz. For a mass cut of $M > 10^{12.5}\,h^{-1}\,{\rm M}_\odot$, the best-fitting centre is incorrect and is identified at 150 kHz. We also find that the deviation from the expected spectra is the largest for this case, where both the height and the width of the spectra are considerably different than the expected curve. The quality of fits is similar for the other two models.

We now move on to quantify the quality of the recovered spectra by doing a likelihood analysis, where we marginalize over the centre $\nu_{\rm bf}$ and plot the 1σ, 2σ and 3σ contours for the remaining two parameters, the width $\Delta\nu_{\rm bf}$ and the height $N_{\rm bf}$ of the stacked spectra. This is shown in Fig. 8. The columns represent the models and the rows are for the three mass cuts. The dotted circle is the best-fitting value of the width and height. The black contours are for the conservative noise of 420 μJy and the blue contours are for the optimistic noise of 71 μJy. The filled diamond is the expected value of the mock spectra without noise, whereas the open square is the same without subhaloes. In all cases, the width and height for the spectra without subhaloes are smaller than for the ones with subhaloes, as was discussed in Section 4.1. This is shown again for reference. For both noise levels, we see that the contours are oriented in a manner showing an anticorrelation between height and width. This is expected since the product of the two determines the mass of the object. This degeneracy which determines the mass of the object is shown in the solid ochre line passing through the expected value of the mock spectra. An incorrect combination of the two would give the same average H I mass per halo.

We find that for the optimistic noise, the quality of the fit is extremely good and the best-fitting values are within 1σ of the expected values for the smallest mass threshold of $M > 10^{11.4}\,h^{-1}\,{\rm M}_\odot$ and is within 3σ for the other two mass cuts. However, satellites below the threshold mass and contributing to the H I mass of the target halo can be more strongly discriminated with the larger mass cut. The difference being the largest for model 3 and the least for model 2 as discussed in Section 4.1. We indeed find that the stacked spectra with and without features of satellite galaxies can be discriminated by more than 7σ for the two larger mass cuts and by 4σ for the smaller mass cut, in our model. The contribution of satellites

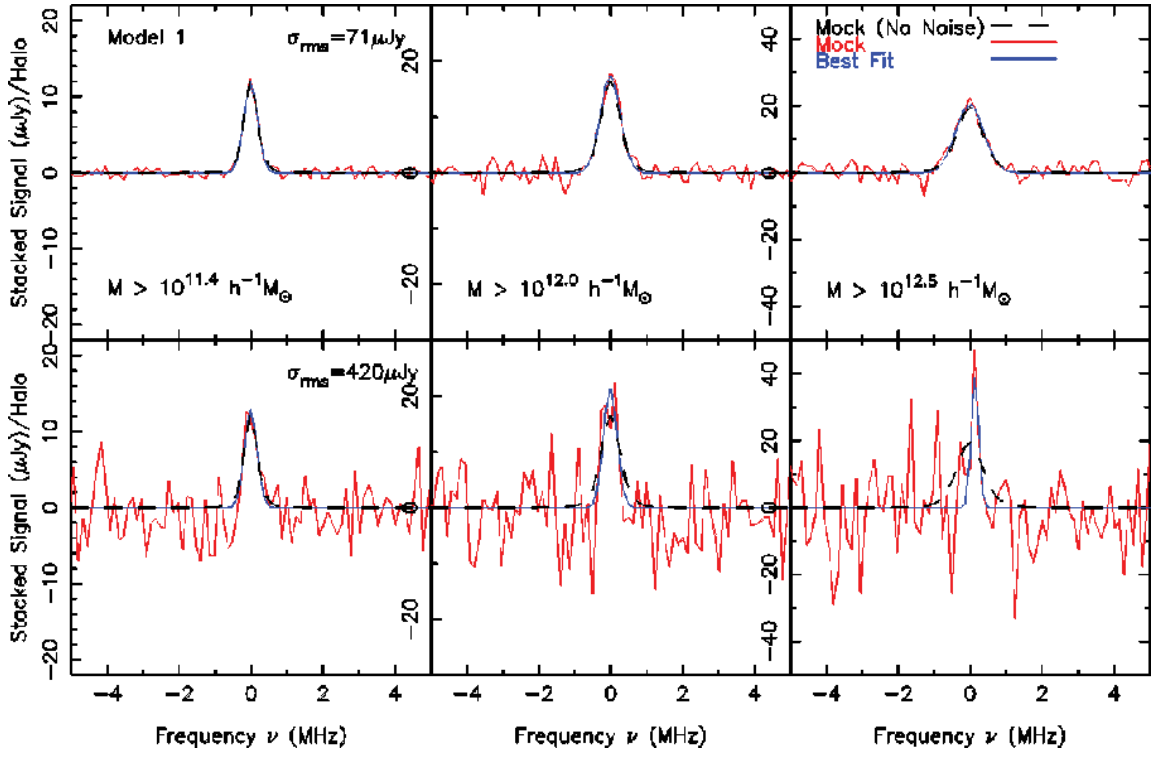

Figure 7. Best-fitting spectra for model 1 by fitting a Gaussian to the mock spectra with rms noise of 71 μJy (top) and 420 μJy (bottom), for the three mass cuts $M \geq 10^{11.4}\,h^{-1}\,{\rm M}_\odot$ (left), $M \geq 10^{12.0}\,h^{-1}\,{\rm M}_\odot$ (centre) and $M \geq 10^{12.5}\,h^{-1}\,{\rm M}_\odot$ (right). All three fits have $\chi^2_{\rm red} \simeq 1$.

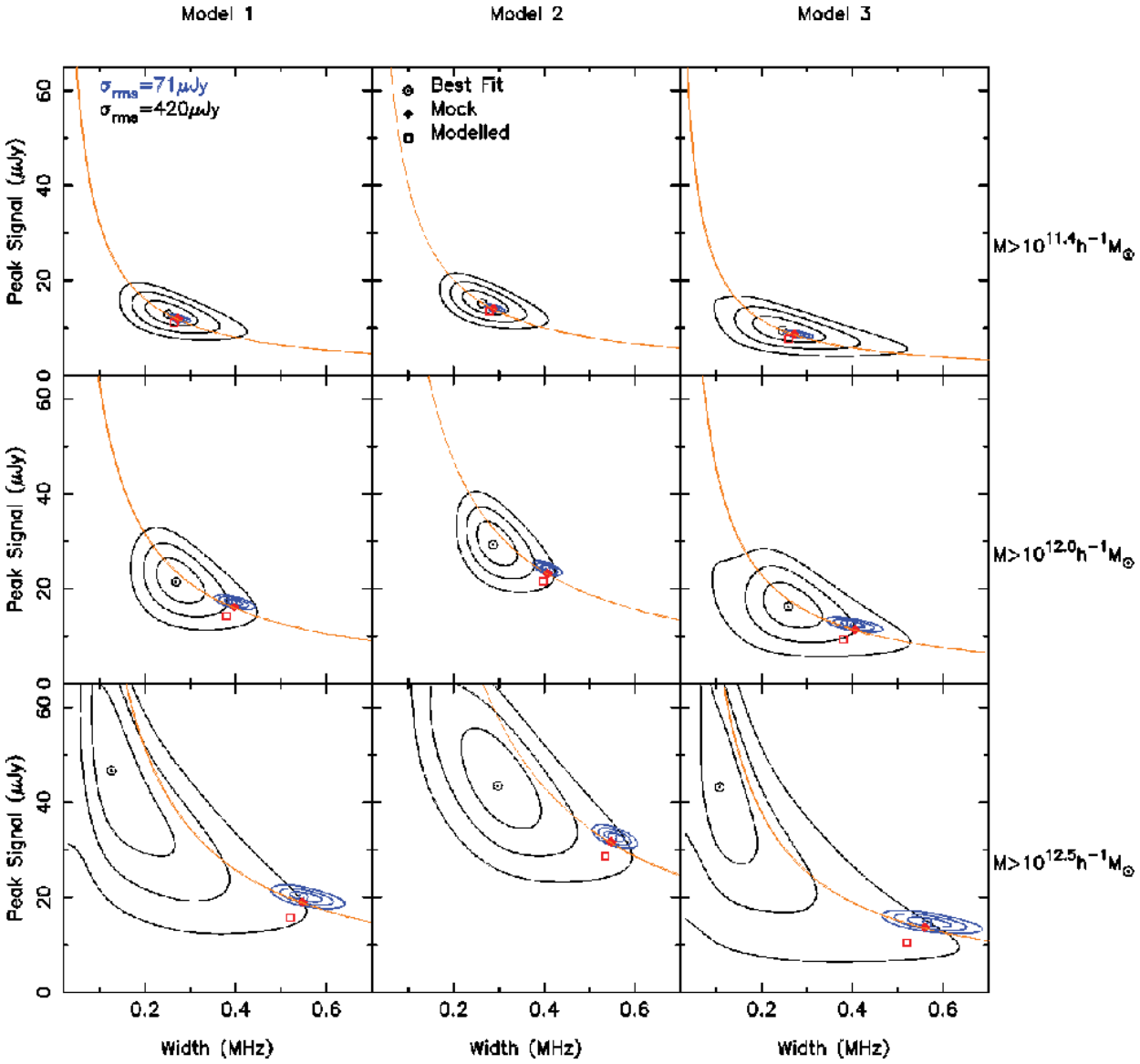

Figure 8. Confidence contours for width and height of the fitted Gaussians for the three models (columns) and the three mass cuts $M \geq 10^{11.4}\,h^{-1}\,\mathrm{M}_{\odot}$, $M \geq 10^{12.0}\,h^{-1}\,\mathrm{M}_{\odot}$ and $M \geq 10^{12.5}\,h^{-1}\,\mathrm{M}_{\odot}$ (rows). The 1σ, 2σ and 3σ contours are shown for both the conservative noise of 420 μJy (black) and for the optimistic noise of 71 μJy (blue). The dotted circles are the best-fitting values from the mock spectra. The open square is the expected point without subhaloes, and the diamond is the expected point with subhaloes, i.e. mock spectra without noise. The solid ochre line shows the combinations of height and width which give the same mass as the expected average H I mass of the halo from the mock spectra.

in the lowest mass cut corresponds to objects missing in the optical survey.

The GMRT will therefore be sensitive to subhaloes that are undetected in the optical survey (although optical stacking would be able to detect them). Inferring what their fractional contribution is could be carried out in various model-dependent ways. One can look at specific model predictions (as has been done in this paper) to compare to the stacked signal. One could instead determine how satellite galaxies populate the central halo, i.e. measure the halo occupation distribution, from a different approach. The latter approach should be feasible in a statistical 21-cm survey where one observes the 21-cm power spectrum (or the correlation function) out to small non-linear scales and infers the halo occupation distribution (HOD) from it (Wyithe & Brown 2010). This was done with the correlation function of the HIPASS galaxies at $z \simeq 0$ (Wyithe et al. 2009). Recently Bagla et al. (2010) showed that a stand-alone statistical detection of 21-cm clustering would not be feasible with the GMRT or the Murchison wide-field array (MWA) and will have to wait for future instruments.

For the conservative noise of 420 μJy, the best fit and the expected value lie within 1σ for a mass cut of $M > 10^{11.4}\,h^{-1}\,\mathrm{M}_{\odot}$. This degrades to 2σ and 3σ for the larger mass cuts. In this case, since the noise is larger, the error contours are also broader compared to a noise level of 71 μJy. We also find that the best-fitting value systematically veers off the line of constant mass in the direction of lower mass as the threshold mass is increased. This trend is also seen for the lower noise but in the direction of higher mass, but is less prominent. The realization of noise decides in which direction the best-fitting value moves when noise becomes important, since it may underpredict or overpredict the H I mass. We cannot distinguish the effect of satellites on the spectra with the conservative noise, unlike the optimistic case. However, as mentioned before, since the

best-fitting value for the two lower mass cuts still lie near the line of constant mass, we would not get the cumulative H I mass wrong, even though the shape of the spectra differs from the true shape for $M > 10^{12.5}\,h^{-1}\,\mathrm{M}_{\odot}$ as seen in the bottom right panel of Fig. 7.

A simpler approach to determine the H I mass from the stacked spectra is to integrate it over a finite frequency range to obtain an integrated flux. The total H I mass for the stacked galaxies is proportional to the integrated flux. The errors in the integrated flux can be obtained by first randomizing the positions of the haloes and then stacking their spectra. We find that for the optimistic noise of $\sigma_{\rm rms} = 71\,\mu$Jy, the H I mass estimated from this method compares well with that expected from the model. However, the errors on the H I mass are smaller as compared to that obtained from the maximum likelihood method discussed previously. For the conservative noise this method is not reliable. As noted earlier, the realization of noise for the conservative case is negatively biased in the stacked spectra and the best-fitting value of H I mass is underpredicted. This can be seen in the bottom panel of Fig. 7 and in Fig. 8. Due to this reason the integrated flux in this case is negative for $M \geq 10^{11.4}\,h^{-1}\,\mathrm{M}_{\odot}$ and $M \geq 10^{12.0}\,h^{-1}\,\mathrm{M}_{\odot}$ for models 1 and 3. For model 2, the H I mass estimate is positive but a factor of 10 lower than what is expected. In all three models, the H I mass estimate is severely suppressed for $M \geq 10^{12.5}\,h^{-1}\,\mathrm{M}_{\odot}$ and the errors on the H I mass are not reliable. Since a prior of a positive definite signal is assumed in the maximum likelihood method, the estimated H I mass and errors are more robust and not very sensitive to the noise. On the other hand, since the second method does not assume any priors the results are very sensitive to the level of noise. In the following sections, we only discuss our results in the context of the maximum likelihood method.

The rms fluctuations in the shape of the average spectra when considering all the subvolumes are a few per cent and below the fluctuations in total mass. This happens because we fit the average spectra of haloes above the mass threshold and not the total spectra. The number of haloes above a certain mass cut fluctuates more strongly as an increasing function of this mass cut. Therefore, the effect of cosmic variance is larger in the mass function as compared to the average spectra. We will revisit the issue of cosmic variance on the estimates of the H I mass function in the next section. We do not plot the errors due to cosmic variance in Fig. 8, since they are smaller than the size of the symbols.

5.3 Subsamples and constraints on the cumulative H I mass

We now discuss the extent to which the cumulative H I mass can be constrained with the GMRT and DEEP2. To obtain the H I mass per halo, or the cumulative H I mass, we need to invert equation (5). We assume a mean redshift $\bar{z}$ and a mean luminosity distance $\bar{D}_{\rm L}$ of our survey, which we take to be at the centre of our subvolume along the redshift direction. The total H I mass is then proportional to the height and the width of the fitted Gaussian and the number of haloes above the mass threshold. The error in the H I mass is hence dependant on both: the errors on the height and the width. To obtain the error on either height or width, we further marginalize our likelihood function over the other parameter and compute the 1σ errors on them.

We present the constraints on the cumulative H I mass in Fig. 9 for both the optimistic noise of 71 μJy (left) and the conservative noise of 420 μJy (right). The total H I mass for haloes above the cut-off mass of the halo has been plotted as a function of cut-off mass of the halo. The uncertainty of the best-fitting parameters due to noise as well as fluctuations due to cosmic variance have both been included in the error bars, and were added in quadrature. The contribution of each is shown in Table 3. The solid line is the expected cumulative H I mass and the dashed line is the same without satellites.

The effect of cosmic variance should be more pronounced for rarer or more massive objects. This is indeed the case, as is seen in Table 3, where we find that the fluctuations due to cosmic variance increase with increasing threshold mass for all the three models, the effect being largest for model 2 followed by model 1 and model 3, consistent with the discussion in Section 3.3.

In the optimistic case, the cumulative H I mass can be well constrained over the entire range of masses that we consider. Note that in this case the best-fitting points lie systematically above the cu-

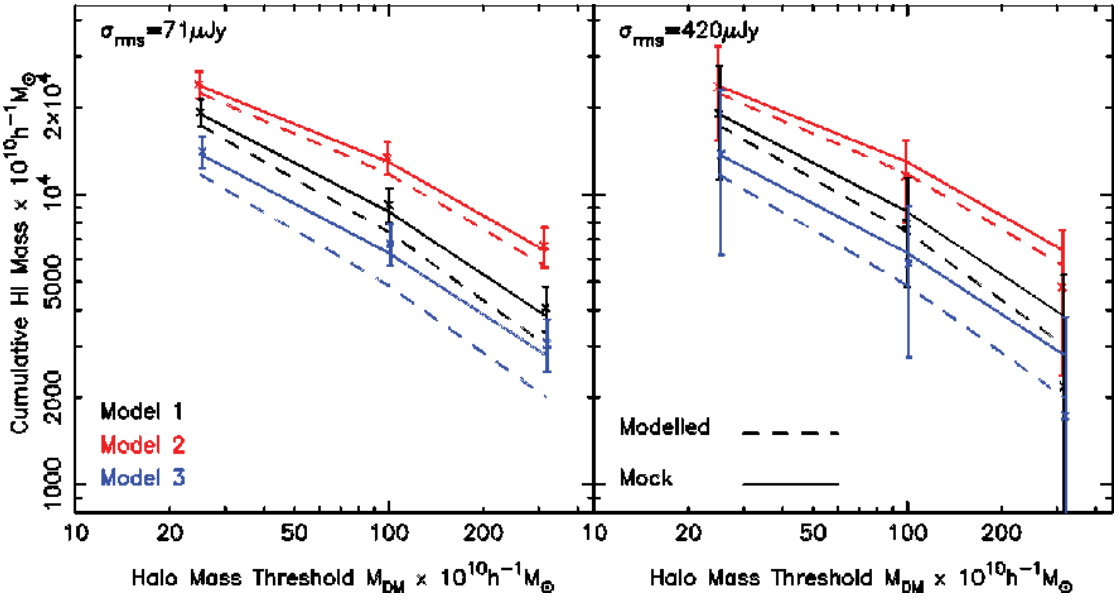

Figure 9. The recovered cumulative H I mass for the three models with the optimistic noise of $\sigma_{\rm rms} = 71$ μJy (left) and the conservative noise of $\sigma_{\rm rms} = 420$ μJy (right). The expected cumulative H I mass with subhaloes (solid line) and without subhaloes (dashed line) are also drawn for comparison. Data points were computed from the mock spectra.

Table 3. Break-up of errors on the cumulative H I mass due to cosmic variance and noise for models (columns) and the three mass cuts that we consider. The first three rows are the per cent fluctuations due to cosmic variance for the three mass cuts. Due to lack of space we change the notation of masses, e.g. $M_{11.4} \equiv 10^{11.4}\,h^{-1}\,\mathrm{M}_{\odot}$. The next three (filled) rows are errors in mass estimates due to the optimistic noise of 71 μJy and the final three (filled) rows are for errors in mass estimates for the conservative noise of 420 μJy.

Errors	Model 1	Model 2	Model 3
$\sigma_{\rm cosm}(M > M_{11.4})$	8.63 per cent	9.30 per cent	8.59 per cent
$\sigma_{\rm cosm}(M > M_{12.0})$	10.85 per cent	11.43 per cent	10.87 per cent
$\sigma_{\rm cosm}(M > M_{12.5})$	13.56 per cent	14.10 per cent	13.58 per cent
$\sigma_{\rm rms} = 71$ μJy			
$\sigma_{M_{\rm HI}}(M > M_{11.4})$	6.47 per cent	5.23 per cent	9.37 per cent
$\sigma_{M_{\rm HI}}(M > M_{12.0})$	8.55 per cent	5.91 per cent	12.11 per cent
$\sigma_{M_{\rm HI}}(M > M_{12.5})$	11.41 per cent	6.87 per cent	15.34 per cent
$\sigma_{\rm rms} = 420$ μJy			
$\sigma_{M_{\rm HI}}(M > M_{11.4})$	42.23 per cent	34.81 per cent	60.04 per cent
$\sigma_{M_{\rm HI}}(M > M_{12.0})$	40.18 per cent	29.82 per cent	53.62 per cent
$\sigma_{M_{\rm HI}}(M > M_{12.5})$	108.97 per cent	52.05 per cent	135.63 per cent

mulative H I mass from the mock spectra, which can be attributed to the noise, as we discussed in the previous section. We had seen in Fig. 8 that the contribution of satellites even for the lowest mass cut could be distinguished at the 3σ level when we look at the stacked spectra. This is not the case for the cumulative H I mass, where the cosmic variance is often more dominant than the errors due to noise. We find that the modelled cumulative H I mass is within 1σ of the best-fitting cumulative H I mass with satellites for model 2 over the entire mass range. This is not so for model 3, where the modelled cumulative H I mass is well beyond the 1σ from the mock cumulative H I mass over the entire mass range that we consider, since the effect of satellites is more pronounced. In model 1, the modelled cumulative H I mass is within the 1σ errors of the mock cumulative H I mass for $M > 10^{11.4}\,h^{-1}\,\mathrm{M}_{\odot}$ and beyond it for the larger mass cuts. From Table 3, we compute the detection significance (including cosmic variance) for the optimistic noise. We find it is the highest for model 2, being 9.4σ for $M > 10^{11.4}\,h^{-1}\,\mathrm{M}_{\odot}$ and 11.6σ for $M > 10^{12.5}\,h^{-1}\,\mathrm{M}_{\odot}$. For models 1 and 3, the numbers are $(9.3\sigma, 5.6\sigma)$ and $(7.9\sigma, 4.9\sigma)$, respectively.

We now move on to the case of the conservative noise in the right-hand panel of Fig. 9. The best-fitting points lie systematically below the mock cumulative H I mass, in this case, due to the different realization of noise than in the optimistic case. Here the uncertainties due to noise are much larger than those due to cosmic variance. The modelled cumulative H I mass is well within 1σ of the mock cumulative H I mass, hence the effect of satellites cannot be seen. We find a 1.7–3σ detection for mass cuts in the range $10^{11.4}\,h^{-1}\,\mathrm{M}_{\odot} < M < 10^{12.0}\,h^{-1}\,\mathrm{M}_{\odot}$. A detection is not a possible for the larger mass cut of $M > 10^{12.5}\,h^{-1}\,\mathrm{M}_{\odot}$ for models 1 and 3, whereas a weak detection is possible for model 2 for this mass cut.

6 DISCUSSION AND CONCLUSIONS

In this paper, we have studied the prospects for detecting H I in emission at $z \simeq 1$. This is a crucial epoch in the study of galaxy formation, since the cosmic SFR starts to decline around this time and the missing link in observations is an accurate census of cold gas, which fuels star formation, at these redshifts and beyond (for more discussion of the importance of this issue, see e.g. Putman et al. 2009). We make a case that an existing instrument like the GMRT can put strong constraints on the amount of cold gas contained in galaxies, when it is combined with a survey like DEEP2. In this work, we have only focused on the overlapping volume of DEEP2 and GMRT, which represents a quarter of the total DEEP2 volume. Our study is representative of what might be achievable by combining the already existing optical data and the presently operational radio interferometers.

The H I signal is too weak in emission for the detection of individual objects at $z \simeq 1$. However, this can be circumvented by a stacking strategy, similar to Lah et al. (2007, 2009), which we here apply to look at the prospects of detection. Our conclusions are as follows.

(i) We find that a detection of H I in emission at redshifts of $z \simeq 1$ is possible even with existing instruments like the GMRT when combined with the DEEP2 survey. Such an observation will be able to constrain the cumulative H I mass in the halo mass range $10^{11.4}\,h^{-1}\,\mathrm{M}_{\odot} \leq M \leq 10^{12.5}\,h^{-1}\,\mathrm{M}_{\odot}$. The detection significance is in the range of 5–12σ for an optimistic noise level of 71 μJy. One may need 300–400 h of observation if one were to target the DEEP2 field between $1.18 < z < 1.3$, and twice this time if one were to target up to $z \sim 1.4$.

(ii) The models that we consider are consistent with recent observations of Chang et al. (2010), who computed the cross-correlation of the density field of DEEP2 galaxies and the 21-cm intensity field with the GBT. However, these observations allow for all the three models that we consider. On the other hand, we find that using the stacking technique it will be possible to discriminate between the different scenarios with an instrument like the GMRT, at least for the optimistic level of noise.

(iii) Combining our estimates of H I bias with the observations of Chang et al. (2010), we put a constraint on the cosmic H I fraction at $z \simeq 0.8$ to be $\Omega_{\rm HI} = (1.03 \pm 0.28) \times 10^{-3}$ for the reference model 1. The estimates on $\Omega_{\rm HI}$ for the other models that we consider are similar and consistent with $\Omega_{\rm HI} = 10^{-3}$.

(iv) We find that undetected satellites in the optical produce a non-negligible contribution to the stacked H I spectra. Their signature is better seen in the stacked spectra rather than in the cumulative H I mass, since we integrate over one parameter, i.e. the width of the spectra, to obtain the cumulative H I mass. For a noise of 71 μJy, features of satellites can be seen at the 4σ level in the stacked spectra for a mass threshold of $M \geq 10^{11.4}\,h^{-1}\,\mathrm{M}_{\odot}$. This detection significance for satellites increases by more than 7σ for $M \geq 10^{12.0}\,h^{-1}\,\mathrm{M}_{\odot}$ (see e.g. Figs 8 and 9). In comparison, the cumulative H I mass discriminates satellites at the $\sim 1\sigma$ level.

(v) We have also considered a much higher level of noise, i.e. 420 μJy, which should represent an upper bound on noise in the GMRT. With this amount of noise, a detection of the cumulative H I mass is possible at the 1.7–3σ level. We expect that the real detection significance is bracketed by the optimistic and conservative noise levels.

(vi) For the higher noise, the effect of satellites on the stacked spectra can be seen only at the 1–3σ level across the ranges of mass that we consider. The best-fitting parameters of the spectra however are incorrect for the larger mass cuts when compared to the theoretical numbers.

(vii) Cosmic variance affects the cumulative H I mass more strongly than the average stacked spectra. For this reason, if H I is populated in haloes according to model 2 one cannot quantify

the effect of subhaloes on the cumulative H I mass due to the effect of cosmic variance. For models 1 and 3, cosmic variance does not swamp the errors due to noise.

One can use the stacking strategy to independently probe $\Omega_{\rm H\,I}$ (Lah et al. 2009). This is not the case in the cross-correlation approach which constrains $br\Omega_{\rm H\,I}$. As in Lah et al. (2007), it would be useful to also target a subset of galaxies in DEEP2 whose SFR has been measured. This would provide the link between the SFR and the amount of cold gas in galaxies and provide insight into models of galaxy formation. Since spectroscopic surveys are accurate but expensive, it would be worthwhile to first try this stacking strategy on future surveys like the large synoptic survey telescope (LSST), which are designed to give photometric redshifts of $\simeq 10^{10}$ galaxies. Photometric redshifts are more prone to errors, but it has to be seen if the larger sample of a photo-z survey like LSST could beat down the noise by its sheer number of objects.

In this study, we have modelled the H I in all the haloes, centrals and satellites, and we have seen how the satellite population affects the cumulative H I mass as well as the stacked H I profile. The possibility to see the effect of satellites missing in an optical survey in the corresponding 21-cm survey is an exciting prospect. On the one hand, we find that stacking can distinguish between models, but the effect of satellites on the stacked profile is model-dependant, and to see their effect one may need to combine it with the cross-correlation approach. In the cross-correlation method, the optical density field does not contain all the satellites, whereas the H I intensity field does. If we use the same mass threshold when constructing the H I intensity field, one naively expects a stronger cross-correlation between the two fields. A preliminary investigation shows that this is indeed the case. We also expect that the H I bias and stochasticity will be sensitive to subhaloes. A combination of both approaches would shed light on both the model and the contribution of satellites.

The other approach is to observe the autocorrelation function or the power spectrum of H I, and to constrain the HOD of H I galaxies (Wyithe & Brown 2010) from it. Such an inferred model of HOD when combined with a direct detection as is done here could reveal the contribution of the satellite population on the total signal. We will look into these aspects of the analysis in a forthcoming paper.

Currently operational radio instruments – both single dish and interferometers – have the capability to detect H I in emission at $z \simeq 1$, as already demonstrated by Chang et al. (2010). We explored the potential of these complementary strategies. In particular, we studied in detail the efficiency of stacking, possible only with interferometers. In the near future, we expect larger optical galaxy samples at $z \simeq 1$ and radio observations with wider field of views and spectral coverage using upcoming radio instruments (e.g. Johnston et al. 2007). This observational progress will enable a better determination of the H I signal using either of the strategies, thereby substantially improving our estimate of the H I content of galaxies at $z \simeq 1$.

ACKNOWLEDGMENTS

We would like to thank Kevin Bandura and Jeff Peterson for useful discussions on the analysis of their recent paper. We would like to thank Jeffrey A. Newman for useful discussions. The authors would like to thank the anonymous referee for suggestions which helped improve the paper. This work was supported by NSF award OCI-0749212. This research was supported by an allocation of advanced computing resources provided by the National Science Foundation. The computations were performed on Kraken, Athena, or Nautilus at the National Institute for Computational Sciences (http://www.nics.tennessee.edu).

REFERENCES

Bagla J. S., Khandai N., Datta K. K., 2010, MNRAS, 407, 567
Bharadwaj S., Sethi S. K., 2001, JA&A, 22, 293
Bharadwaj S., Sethi S. K., Saini T. D., 2009, Phys. Rev. D, 79, 083538
Catinella B., Haynes M. P., Giovanelli R., Gardner J. P., Connolly A. J., 2008, ApJ, 685, L13
Chang T.-C., Pen U.-L., Peterson J. B., McDonald P., 2008, Phys. Rev. Lett., 100, 091303
Chang T.-C., Pen U.-L., Bandura K., Peterson J. B., 2010, Nat, 466, 463
Coil A. L. et al., 2008, ApJ, 672, 153
Conroy C., Wechsler R. H., Kravtsov A. V., 2006, ApJ, 647, 201
Conroy C. et al., 2007, ApJ, 654, 153
Fu J., Guo Q., Kauffmann G., Krumholz M. R., 2010, MNRAS, 409, 515
Gardner J. P., Katz N., Hernquist L., Weinberg D. H., 2001, ApJ, 559, 131
Gerke B. F. et al., 2007, MNRAS, 376, 1425
Haehnelt M. G., Steinmetz M., Rauch M., 2000, ApJ, 534, 594
Hopkins A. M., 2004, ApJ, 615, 209
Johnston S. et al., 2007, Publ. Astron. Soc. Australia, 24, 174
Kanekar N., Prochaska J. X., Ellison S. L., Chengalur J. N., 2009, MNRAS, 396, 385
Kim H.-S., Baugh C. M., Benson A. J., Cole S., Frenk C. S., Lacey C. G., Power C., Schneider M., 2011, MNRAS, doi:10.1111/j.1365-2966.2011.18556.x
Lah P. et al., 2007, MNRAS, 376, 1357
Lah P. et al., 2009, MNRAS, 399, 1447
Marín F. A., Gnedin N. Y., Seo H.-J., Vallinotto A., 2010, ApJ, 718, 972
Noterdaeme P., Petitjean P., Ledoux C., Srianand R., 2009, A&A, 505, 1087
Obreschkow D., Rawlings S., 2009a, ApJ, 696, L129
Obreschkow D., Rawlings S., 2009b, MNRAS, 400, 665
Obreschkow D., Croton D., De Lucia G., Khochfar S., Rawlings S., 2009a, ApJ, 698, 1467
Obreschkow D., Klöckner H.-R., Heywood I., Levrier F., Rawlings S., 2009b, ApJ, 703, 1890
Péroux C., Dessauges-Zavadsky M., D'Odorico S., Sun Kim T., McMahon R. G., 2005, MNRAS, 363, 479
Pontzen A. et al., 2008, MNRAS, 390, 1349
Power C., Baugh C. M., Lacey C. G., 2010, MNRAS, 406, 43
Prochaska J. X., Herbert-Fort S., Wolfe A. M., 2005, ApJ, 635, 123
Putman M. E. et al., 2009, Astro2010: The Astronomy and Astrophysics Decadal Survey. Science White Papers, 241
Rao S. M., Turnshek D. A., 2000, ApJS, 130, 1
Rao S. M., Turnshek D. A., Nestor D. B., 2006, ApJ, 636, 610
Springel V., 2005, MNRAS, 364, 1105
Springel V., White S. D. M., Tormen G., Kauffmann G., 2001, MNRAS, 328, 726
Springel V. et al., 2005, Nat, 435, 629
Storrie-Lombardi L. J., McMahon R. G., Irwin M. J., 1996, MNRAS, 283, L79
Thompson A. R., Moran J. M., Swenson G. W., Jr, 2001, Interferometry and Synthesis in Radio Astronomy, 2nd edn., Wiley, New York
Wolfe A. M., Gawiser E., Prochaska J. X., 2005, ARA&A, 43, 861
Wyithe J. S. B., Brown M. J. I., 2010, MNRAS, 404, 876
Wyithe S., Brown M. J. I., Zwaan M. A., Meyer M. J., 2009, preprint (arXiv:0908.2854)
Zwaan M. A., Meyer M. J., Staveley-Smith L., Webster R. L., 2005, MNRAS, 359, L30

This paper has been typeset from a TEX/LATEX file prepared by the author.